

AD _____

Award Number: W81XWH-04-1-0229

TITLE: Non-Invasive Monitoring for Optimization of Therapeutic
Drug Delivery by Biodegradable Fiber to Prostate Tumor

PRINCIPAL INVESTIGATOR: Dan Popa, Ph.D.
Hanli Liu, Ph.D.
Liping Tang, Ph.D.

CONTRACTING ORGANIZATION: The University of Texas at Arlington
Arlington, TX 76019

REPORT DATE: February 2007

TYPE OF REPORT: Annual

PREPARED FOR: U.S. Army Medical Research and Materiel Command
Fort Detrick, Maryland 21702-5012

DISTRIBUTION STATEMENT:

Approved for public release; distribution unlimited

The views, opinions and/or findings contained in this report are those of the author(s) and should not be construed as an official Department of the Army position, policy or decision unless so designated by other documentation.

REPORT DOCUMENTATION PAGE				Form Approved OMB No. 0704-0188	
Public reporting burden for this collection of information is estimated to average 1 hour per response, including the time for reviewing instructions, searching existing data sources, gathering and maintaining the data needed, and completing and reviewing this collection of information. Send comments regarding this burden estimate or any other aspect of this collection of information, including suggestions for reducing this burden to Department of Defense, Washington Headquarters Services, Directorate for Information Operations and Reports (0704-0188), 1215 Jefferson Davis Highway, Suite 1204, Arlington, VA 22202-4302. Respondents should be aware that notwithstanding any other provision of law, no person shall be subject to any penalty for failing to comply with a collection of information if it does not display a currently valid OMB control number. PLEASE DO NOT RETURN YOUR FORM TO THE ABOVE ADDRESS.					
1. REPORT DATE 01-02-2007		2. REPORT TYPE Annual		3. DATES COVERED 1 Feb 2006 – 31 Jan 2007	
4. TITLE AND SUBTITLE Non-Invasive Monitoring for Optimization of Therapeutic Drug Delivery by Biodegradable Fiber to Prostate Tumor				5a. CONTRACT NUMBER	
				5b. GRANT NUMBER W81XWH-04-1-0229	
				5c. PROGRAM ELEMENT NUMBER	
6. AUTHOR(S) Dan Popa, Ph.D., Hanli Liu, Ph.D., Liping Tang, Ph.D. Email: popa@uta.edu				5d. PROJECT NUMBER	
				5e. TASK NUMBER	
				5f. WORK UNIT NUMBER	
7. PERFORMING ORGANIZATION NAME(S) AND ADDRESS(ES) The University of Texas at Arlington Arlington, TX 76019				8. PERFORMING ORGANIZATION REPORT NUMBER	
9. SPONSORING / MONITORING AGENCY NAME(S) AND ADDRESS(ES) U.S. Army Medical Research and Materiel Command Fort Detrick, Maryland 21702-5012				10. SPONSOR/MONITOR'S ACRONYM(S)	
				11. SPONSOR/MONITOR'S REPORT NUMBER(S)	
12. DISTRIBUTION / AVAILABILITY STATEMENT Approved for Public Release; Distribution Unlimited					
13. SUPPLEMENTARY NOTES Original contains colored plates: ALL DTIC reproductions will be in black and white.					
14. ABSTRACT Chemotherapeutic drugs delivered by systematic administration exhibit great toxicity; patients have to endure suffering from frequent injection or low dose IV treatment. Thus controlled release and of these drugs and real-time monitoring of the effects of the drug can be an better treatment modality. The Hypotheses are (1): A near-infrared (NIR) imager can non-invasively monitor the vascular oxygenation and blood volumes in prostate tumors. (2): The dynamic response of prostate tumor oxygenation to the chronic drug delivery can serve as indicator for treatment prognosis. (3): The control of drug delivery rate will have a significant impact on the treatment prognosis. The specific aims of the of the project are: (1): To design and implement a NIR spectroscopic imaging system. (2): To develop imaging of drug concentration and tumor oxygenation. (3): To control the delivery of drug using a novel implantable micropump (IDDS).(4): To study the relationship between drug release rate, tumor oxygen levels and therapeutic outcome. (5): To create appropriate cancer tumor animal models, that will guide the growth of cancer tumor in Copenhagen rats.					
15. SUBJECT TERMS Technology Development, Radiological Sciences, Tumor Therapy Planning and Prognosis, Tumor Physiology Monitoring.					
16. SECURITY CLASSIFICATION OF:			17. LIMITATION OF ABSTRACT	18. NUMBER OF PAGES	19a. NAME OF RESPONSIBLE PERSON
a. REPORT	b. ABSTRACT	c. THIS PAGE			USAMRMC
U	U	U	UU	30	19b. TELEPHONE NUMBER (include area code)

Table of Contents

Introduction.....	3
Body.....	3
Key Research Accomplishments.....	27
Reportable Outcomes.....	27
References.....	29

Introduction

This report presents progress and accomplishment during the third year, between March 1 2006 and February 28 2007. It contains research results from the PI, Dr. Dan Popa, Assistant Professor, Electrical Engineering, UTA, and two co-PI's: Dr. Hanli Liu and Dr. Liping Tang, Professors of BioEngineering Department, UTA. Due to delays in the start of the project and change of PI's, we requested that the project funding be extended for one year, so that remaining research can be completed. Our November 2006 request was approved in February 2007.

Chemotherapeutic drugs delivered by systematic administration exhibit great toxicity; patients have to endure suffering from frequent injection or low dose IV treatment. Thus controlled release of these drugs will be a treatment modality. Moreover, real-time monitoring of the effects of the drug by sensing the dynamic response of the tumor to a particular drug can significantly enhance the therapeutic outcome. The Hypotheses are (1): A near-infrared (NIR) imager can non-invasively monitor the dynamic and chronic distribution of the chemotherapeutic drug, vascular oxygenation, and blood volumes in prostate tumors. (2): The dynamic response of prostate tumor oxygenation to the chronic drug delivery can serve as indicator for treatment prognosis. (3): The control of drug delivery rate will have a significant impact on the treatment prognosis. The original specific aims of this project were:

(Aim 1): To design and implement a NIR spectroscopic imaging system

(Aim 2): To develop 2D tomographic imaging of drug concentration and tumor oxygenation.

(Aim 3): To control the delivery of drug using a novel implantable micropump (IDDS).

(Aim 4): To study the relationship between drug release rate, tumor oxygen levels and therapeutic outcome.

(Aim 5): To create appropriate cancer tumor animal models, that will guide the growth of cancer tumor in Copenhagen rats.

Body of Report

1. Progress on Aims 3 and 4 from PI Popa

A. INTRODUCTION

The central idea of the MEMS IDDS is to utilize the well established principles of intravenous therapy (IV) to deliver controlled amounts a cancer drugs. The reservoir, pump, catheter and associated circuitry will mimic the intravenous fluid bags and catheter. Conventional intravenous therapy relies on positioning the fluid bag to deliver the drug, as in "gravity drip" or expensive Infusion pumps to pump the drug into the circulatory system. These however limit patient mobility by confining them to a bed side infusion set up. The MEMS based IDDS aims to provide all the benefits of conventional IV therapy

with a small implantable pump and provide mobility. We also intend to incorporate telemetry circuitry to control the pump and obtain information from the pump.

MEMS have the advantage of using existing silicon fabrication technologies which can be integrated with CMOS devices while adding the functionality of mechanical systems. The proposed device aims at using these advantages to develop a centralized or localized implantable drug delivery device for chemotherapy by integrating a subcutaneous reservoir, an in-plane Silicon pump and associated circuitry. Research to meet the strict control required for dispensing therapeutic agents at specific intervals of time using micropump has been carried out since the early 1980's. There are a number of different mechanisms that drive a pump. The first micropump to deliver insulin was introduced in 1980 by Jan Smits. Other applications include the use of micropumps in drug delivery for cancer, chronic pain, spasticity, etc. Pumps may be classified as displacement-driven, and dynamic pumps which include centrifugal, electro-hydro-dynamic and electro-osmotic delivery mechanisms. Pumps add mechanical energy to the fluid. If the energy is added in periodic manner they are termed as displacement micropumps and if the energy is added continuously they are called dynamic pumps. In our case, we are developing a displacement micropump, based on an in-plane design and stacked die package.

As we reported last year, the IDDS is fabricated by DRIE on a SOI wafer. In contrast to traditional peristaltic micropump designs, which use an out-of plane pumping diaphragm, the in-plane pump consists of the actuators, diaphragms, reservoir and I/O fluidic valves fabricated in a single layer. Joule heating of the V-beams and lever mechanism amplifies the stroke of the pump. The fluidic path is enclosed by anodic bonding of a PyrexTM glass to the pump die, and the overall fabricated mask layout is shown in Figure 1. The targeted adjustable pump rate is 1-100 $\mu\text{l/min}$, but exact design values for prostate cancer will be determined as an outcome of Aim 4. In addition to the MEMS die enclosed by Pyrex (Level 0 package), the pump must also be interconnected with electronics, power, and RF communication from inside the body. There are multiple levels of packaging, starting from Level 0 (SOI MEMS+Anodic Bonding of Pyrex), Level 1 (Enclosing the pump inside a carrier, and providing appropriate fluidic and electrical interconnects), and Level 2 (System level package by adding electronics, power, and a reservoir). In 2006, we focused on Level 0 and 1 packaging and interconnects of the MEMS die, and in creating a basic Level 2 prototype for testing the micropump with cancer drugs next year.

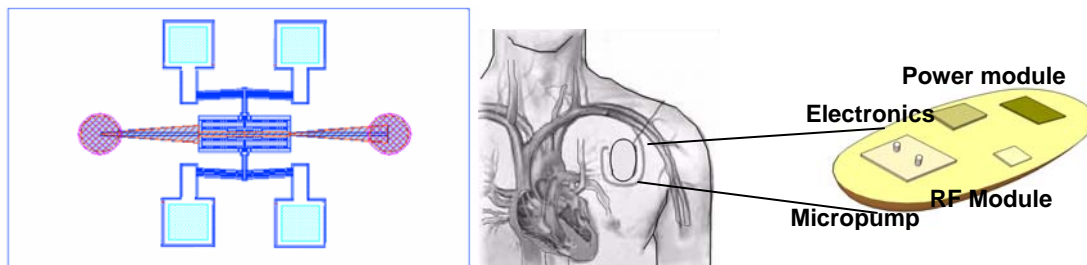


Figure 1: SOI MEMS layout of the in-plane pump (left) and a system level diagram of the whole implantable unit

When this micropump will be eventually tested on human subjects, a reservoir is also needed to ensure that drugs delivered through the implantable micropump can be replenished. Our reservoir is similar in design to the vascular access ports. These ports

have been demonstrated to have good bio-stability and bio-compatibility. For this application, the reservoir should have smooth contours, hold at least 5 ml of the drug and be easily accessible for refilling. A subcutaneous position for the port-like reservoir is targeted for the IDDS, and Ti and Silicone materials will be used for biocompatibility (Fig 2).



Figure 2: Inch-size Titanium and Silicone port reservoirs, refillable through injection.

B. MICROPUMP DESIGN THROUGH MODELING AND SIMULATION

B1. LUMPED MODEL APPROXIMATION FOR FLOW RATE ESTIMATION

In order to guide in the micropump design parameters, we used Finite Element Analysis. Due to limitations of FEA to model electrothermal, displacement and flow effects simultaneously, we also developed a lumped parameter dynamic model to calculate the flow as shown in Fig. 3. Motion obtained by flexing the diaphragm is simplified to the motion of a piston of mass $m = 3 \mu\text{g}$. Based on the finite element model of the actuator and diaphragm the stiffness is $k = 200 \text{ N/m}$ and the actuator force $F = 6 \text{ mN}$ for a voltage input of 15 V was fed into the lumped parameter model.

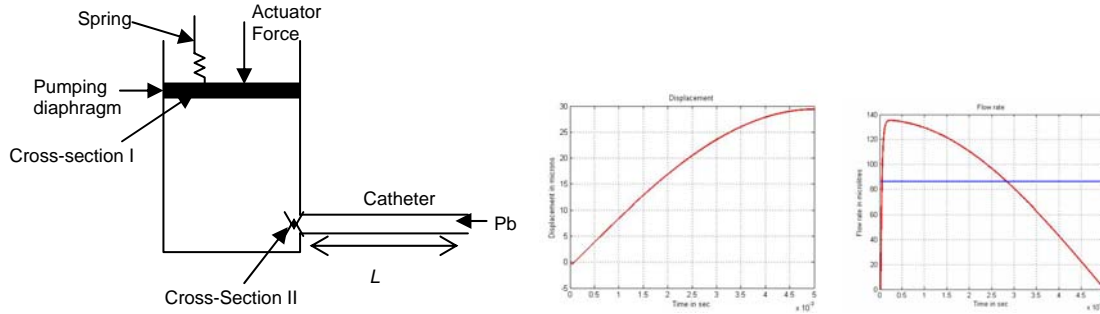


Figure 3: Lumped parameter model used to estimate flow rate of the micropump (left), pump diaphragm displacement and flow plots for one pumping stroke (center and right)

By writing the dynamic equations of motion and the continuity and Bernoulli flow equations we obtain:

$$\begin{aligned}
 m\ddot{x}_1 + b\dot{x}_1 + kx_1 + p_1 A_1 &= F, \\
 A_1 \dot{x}_1 &= A_2 \dot{x}_2, \\
 p_2 + \frac{\rho \dot{x}_2^2}{2} &= p_1 + \frac{\rho \dot{x}_1^2}{2},
 \end{aligned} \tag{1}$$

in which x_1 is displacement of piston, p_1 is pressure below the piston, A_1 is cross-section of the piston equal to 1.44 mm^2 , x_2 is outlet flow velocity, A_2 cross-section of outlet equal to 0.78 mm^2 , ρ is the density of the liquid, b is the diaphragm damping factor. In our simulations, b was chosen to critically damp the system, e.g. $b = 2\sqrt{km}$. The outlet of the pump chamber is connected to a catheter of length L equal to 10 cm and diameter D equal to $500 \text{ }\mu\text{m}$ that connects the pump to the vein. Based on physiological data we assume that the back pressure at the end of the catheter is $P_b=8\text{mmHg}$, therefore a pressure boundary condition for our model is $p_2 = p_b + \Delta p$, where the pressure drop across the catheter of pipe friction coefficient λ is given by the Darcy-Weisbach formula for pressure drop across circular pipes.

$$\Delta p = \lambda \times \frac{l}{D} \times \frac{\rho}{2} \times \dot{x}_2^2, \quad (2)$$

The resulting dynamical equations for the micropump takes the form of a nonlinear lumped model approximate ODE:

$$m\ddot{x}_1 + kx_1 + (p_b + k_3\dot{x}_1^2)A_1 = F. \quad (3)$$

Flow simulations for a micropump/check-valve/catheter system were carried out in *MATLAB*. Assuming a sinusoidal signal to the MEMS actuator with frequency $f = 50\text{Hz}$ (close to the thermal bandwidth of the MEMS actuator), and amplitude $F = 6\text{mN}$ we obtain the output flow rate of the pump.. Simulation results indicate that an average flow rate of $85 \text{ }\mu\text{l/min}$ can be achieved against a venous pressure of 8 mmHg .

B2. EXPERIMENTAL VERIFICATION OF MODELS THROUGH PUMP MOTION CHARACTERIZATION

Experiments were conducted to verify the displacement of the Chevron beam actuator and the pump diaphragm. For this analysis, we used a Veeco Wyko NT1100 DMEMS motion analyzer located at our Texas Microfactory TM Lab, shown in Figure 4. Dynamic analysis was carried out to quantify the displacement of the actuator as a function of time, phase, amplitude and frequency. The amplitude, phase, frequency of the input signal was varied together or in a sequence to describe the complete motion of the MEMS device. The dynamic response of the micropump provides information regarding maximum displacement and resonant frequency. Analysis was carried out with sinusoidal and square wave inputs. The voltage was varied from 8-24V and the frequency from 15-100Hz. For square wave, the duty cycle considered was 20%. The displacement of the chevron beam and the diaphragm was observed. The minimum and maximum displacement of the diaphragm was $2\mu\text{m}$ and $11\mu\text{m}$ respectively. The corresponding frequencies were 70Hz and 45Hz respectively. The cut-off frequency is 40Hz. The motion amplification through the cantilever transmission has been experimentally found to be approximately 5 times.



Figure 4: Veeco Wyko NT1100 Optical Profiling system (left), and a MEMS die being probed on this setup for motion characterization.

Based on the experimental measurements, the diaphragm pumping force was downgraded to 1.17 mN, based on which a flow rate of approximately 30 $\mu\text{L}/\text{min}$ is expected. Typical displacement plots of the diaphragm of the in-plane pump for square wave and sinusoidal input voltages are shown in Figure 5.

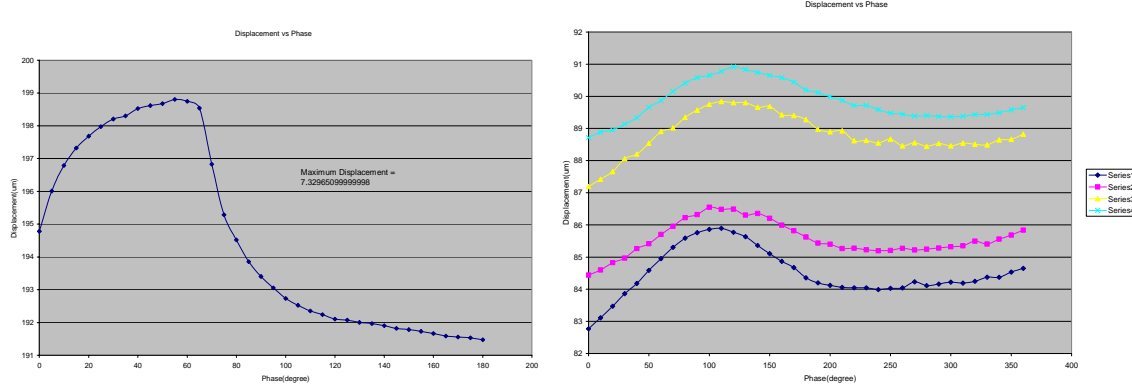


Figure 5: Displacement measurements of pump diaphragm for square wave input (left) and as a function of phase of sinusoidal input (right).

C. MICROPUMP FABRICATION AND PACKAGING

The electrothermal actuator for our micropump is fabricated using a 500 micron thick SOI (Silicon on insulator) wafer. The different elements that constitute the device are voltage pads, V-shaped chevron beams and a center shaft connected to the diaphragm through lever mechanism for stroke amplification (Fig. 6). It consists of six chevron beams on either side of the center shaft. The beams are 1200 μm in length with a cross sectional area of 12 μm x 100 μm with a rib angle of 5.7°. The pump diaphragm is 750 μm in length, 100 μm in height and 50 μm wide. It also consists of 2000 μm x 100 μm x 100 μm (length x width x height) fluidic channel along with a nozzle/diffuser arrangement for flow rectification. The dimensions are based upon the detailed optimization studies. Several wafers with miropump dies have been fabricated at Stanford Nanotechnology Center (SNF) last year and tested/packageged at UTA. A picture of fabricated substrates and Level-0 packaged prototypes are shown in Figure 6.

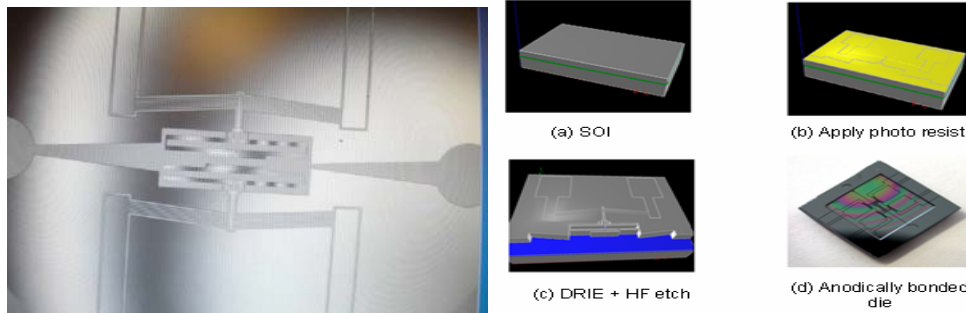


Figure 6: Fabricated SOI in-plane micropump , and a description of Fabrication and Level 0 Packaging steps

In order to increase the reliability of the micropump, the MEMS devices must be packaged appropriately. Packaging provides a platform for component mounting and also protects the device from external damage caused by contamination, moisture and handling. It also serves as the path for heat removal. The anodically bonded pump die is attached to a 1mm thick Kovar plate of dimensions $1500 \times 1500 \mu\text{m}^2$ through a 1mil thick thermal interface material (TIM). Wire bonding is done in order to provide electrical connections for the MEMS die. Lastly, the whole structure is sealed with Kovar metal cap. The schematic of the next packaging level for the die (Level 1) is shown in Fig. 7.

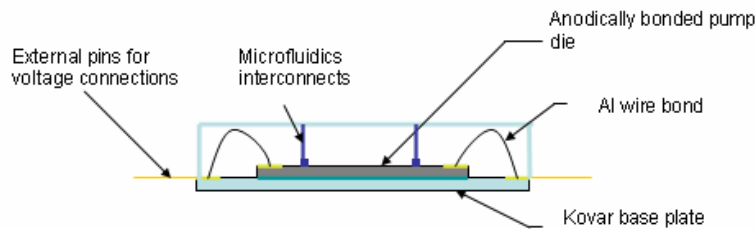


Figure 7: Schematic representation of the packaged pump die (Level 1 packaging).

C1. LEVEL 0 MICROPUMP PACKAGING

The first level of micropump packaging is done using Anodic bonding of the MEMS die with a Pyrex glass chip. This ensures that the fluidic pathways in the pump are created. The technique of bonding Silicon and Glass under the influence of temperature and voltage is known as anodic bonding. The formation of the bond involves the displacement of the Sodium ions in glass by the applied field forming a depletion region at the surface. This highly reactive surface forms a strong chemical bond with the Silicon. Anodic bonding requires very smooth and flat surfaces for bonding. It is also sensitive to contamination. The process conditions are temperature in the range of $200\text{-}500^\circ\text{C}$ and voltage of $700\text{-}1.5\text{kV}$. The bond strength is affected by voids or bubbles formed during the bonding process. It has been determined that the bonding temperature plays a critical role in bonding. Bonding time, potential and load contribute weakly to the bonding strength but are key factors in influencing the speed of bond formation and the area bonded. The anodic bonding set up in our lab involves a hot plate, a pressure fixture and a high voltage source. Experiments were conducted to determine optimal process parameters, and an acceptable process window was found. The conditions for anodic

bonding were temperature of 300-500 °C, and Voltage of 1-1.5 kV for 20-25 minutes, at low or no bonding force. The current flowing through the bonded region was monitored throughout the process and was found to be in the range of 9-20mA. The setup and bonded micropump dies are shown in Figure 8.

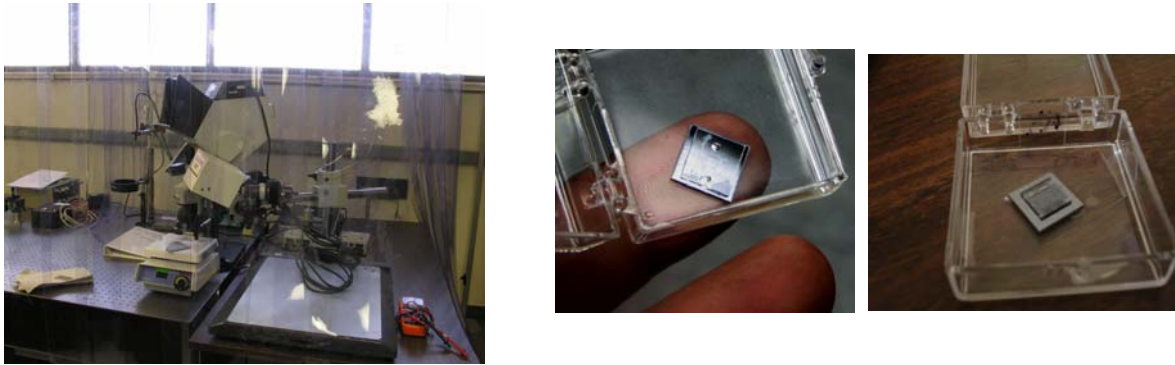


Figure 8: Experimental setup for anodic bonding under a small clean air enclosure (left) and bonded samples (center, right).

In order to provide means for the interconnect through the Pyrex glass of 500 μm in thickness, holes were drilled in the Pyrex die prior to anodic bonding using diamond drill bits 650 μm in diameter to create holes in the range of 700-900 μm at a drill speed of 45,000 rpm. Experiments were conducted to determine acceptable micro drill process parameters and characterize the results. The drilling set up and resulting interconnect holes are shown in Figure 9.

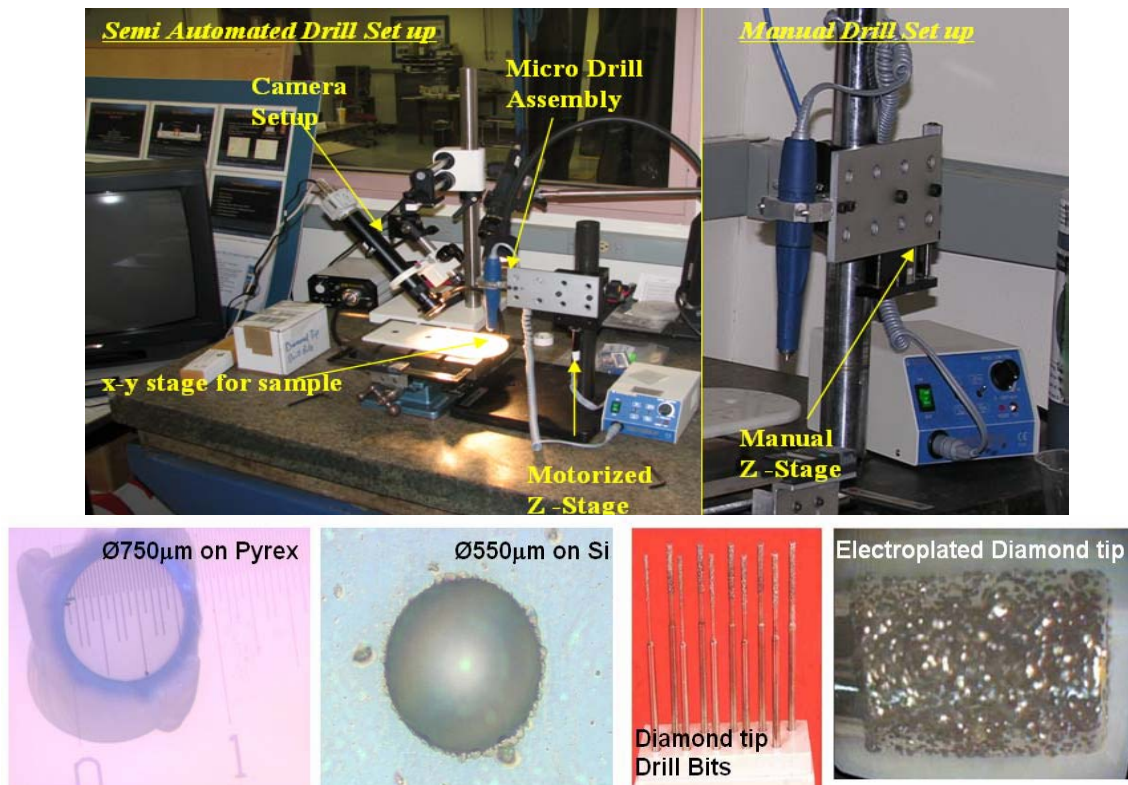


Figure 9: Pyrex micro drilling station and optical measurement of interconnect holes using a Veeco surface profiles

Finally, the fluidic path inside the pump must be contained inside the MEMS device. The SOI MEMS contains $2\mu\text{m}$ leak paths below and above the moving diaphragm in order to actuate, and therefore, it is necessary to contain the fluid flow using a compliant polymeric membrane implemented in the shape of a tube. In order to achieve this, it was proposed that a tube made of Parylene should be embedded in the channel connecting the inlet and outlet of the micropump. The Parylene tube would be in contact with the diaphragm of the pump enabling the pumping of the fluid in the channel contained within the tube. The schematic drawing of the Parylene tube embedded in-plane micropump is as shown in Figure 10.

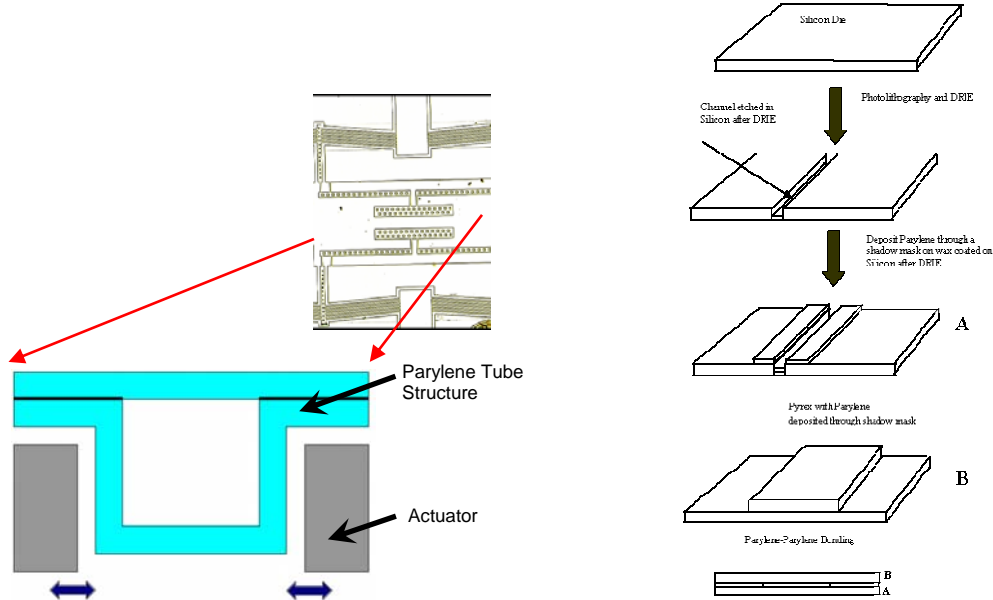


Figure 10: Schematic cross section of a Parylene tube inside the pumping chamber, and fabrication process.

The process of forming the Parylene-Parylene bond is followed by dissolving the molding wax in Toluene to form the tube structure on the Pyrex. This is then aligned and anodically bonded to the SOI micropump die. Experiments have been carried out to fabricate and characterize the fabrication process of the Parylene tube.

C2. LEVEL 1 MICROPUMP PACKAGING

For obtaining a package similar to the diagram in Figure 7, fluidic and electrical interconnects must be fabricated. Fluidic interconnects out of the pumping plane are formed by using PEEK or glass capillary tubes with Silicone tubing. These are bonded to the Pyrex using a fast curing epoxy as shown in Figure 11. In addition, the die stack must be placed inside a carrier package. Because the actuation principle we use is based on a thermal MEMS drive, it is important to study the effects of heat dissipation in order to design the thermal mass of the package and ensure that during device implantation tissues are not exposed to more than a few $^{\circ}\text{C}$ temperature increases.

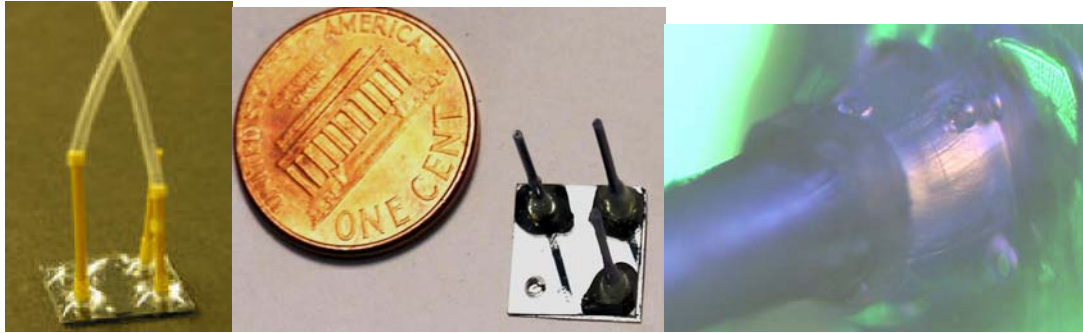


Figure 11: Interconnects on the anodic bonded micropump die

We carried out Level 1 Package thermal analysis using thermal models. An in-depth numerical analysis is performed in order to determine the impact of each variable (air gap, voltage etc) on the maximum device temperature. Analysis was performed using Intellisuite[®]. A 3D model was created using the Intellimask and Intellifab modules. The pump die, Pyrex cap and the package then meshed, and solved in Thermo-Electro-Mechanical module. Approximately 85K nodes were generated. Constant temperature boundary conditions were considered at the voltage pads. A natural convection boundary condition i.e. convective heat transfer coefficient of $10 \text{ W/m}^2\text{°C}$ is considered at the bottom of the package. Voltage (15V to 23V) inputs are defined on one pad, and ground on another as depicted in Figure 12. Typical plots obtained show that packaging has a considerable impact on the MEMS die temperature. Future work will contain designing package geometries and temperature that will ensure optimal operating conditions for the micropump. It was observed that increases in device temperature are proportional to the increase in voltage, air gap thickness and substrate thickness. After packaging, device temperature drops by an average of 20% .

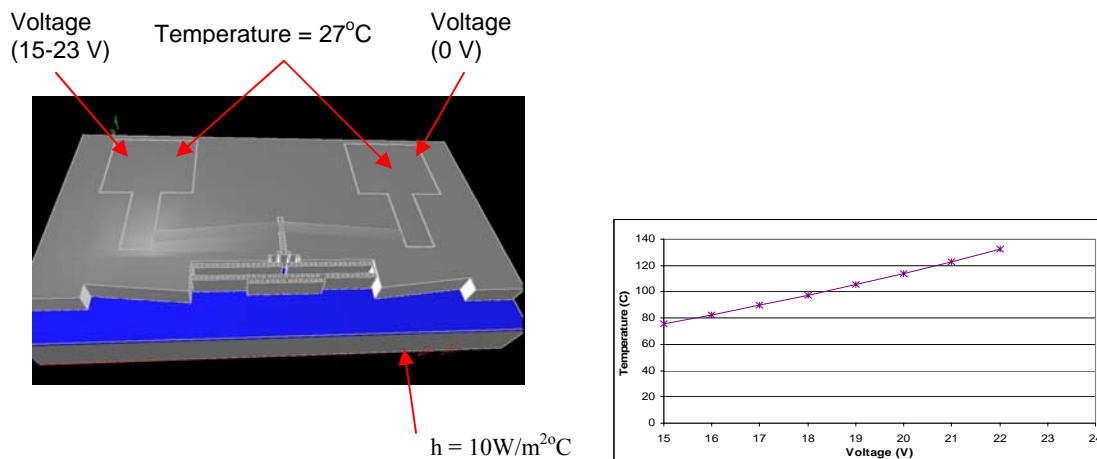


Figure 12: Boundary conditions considered for analysis (left) and plot showing that the beam temperature drops from a few hundred °C for an unpackaged micropump to around 100°C for a packaged pump. The temperature at the outside of the pump is much lower.

C3. LEVEL 2 MICROPUMP PACKAGING

This level of packaging contains the micropump electronic circuitry for logic, driving, RF communication and power.

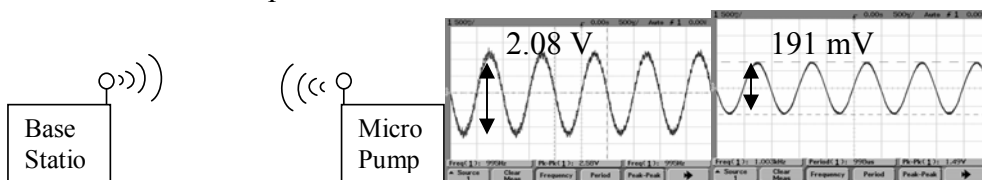


Figure 13: (a) Telemetry set up (b) transmitted and (c) received signal from the telemetry test setup placed 5m apart. The transmitted signal is a 1.2 mV_{p-p} amplified by a factor of 2000 and received signal is 191 mV. The modulated signal is a 1 KHz sine wave with a 433 MHz carrier.

A telemetry module has been set up to ensure a wireless link from the micropump to a base station. The telemetry module consists of a transmitter unit and a receiver unit. The transmitter includes operational amplifiers, amplifier circuit, a miniature antenna and a transmitter chip. The receiver has a receiver chip and signal conditioning circuitry. The antenna chosen is a Copper solenoid of 24 turns. The antenna is soldered on a small printed circuit board with the transmitter chip and lumped elements with operating frequency of 433 MHz. The range of operation is sufficient for the proposed application since the base station will be close to the patient when the physician monitors and programs the implanted unit. Fig. 13 shows the signal received from a transmitter-receiver separated by a distance of 5 m. A 1 KHz sine wave was used to modulate a carrier of 433 MHz. It demonstrated clear communication between the transmitter and receiver. The transmitted signal is 1.2 mV_{p-p} amplified by a factor of 2000. The received signal is filtered by a bandpass filter, 300 Hz – 10 KHz, to reduce noise, especially 60-Hz power line signals and interference from other wireless instruments. The purpose of this demonstration is to show feasibility of telemetry, hence the size of the circuit board has not been optimized. Our goal is to integrate the telemetry and microfluidic devices to deliver a completely implantable drug delivery mechanism.

Several other technical challenges are being investigated. These include power management, size considerations, and control circuit integration. Without taking into account the power required by the RF unit, the estimated power consumption for the target 100 μ l/min delivery rate is in the range of 100-500 mW. This figure is estimated based on the power consumption of the micropump necessary to generate required diaphragm displacements. As a result, commercially available miniature lithium-ion batteries would discharge in less than 48 hours of operation. Therefore, a power management system employing recharging of the power source is necessary in the IDDS. One possibility is recharging from outside of the body using through-skin electrical interconnects. A much better alternative would be wireless power transmission using RF coils. We are in the process of developing a combined miniature RF power recharging and telemetry system for the proposed IDDS.

In order to test the effectiveness of the micropump with cancer drugs and construct appropriate animal models we combined driving circuitry, power and a pump into a table-top hand held unit prototype that is shown in figure 14. Even though this prototype is not yet fully miniaturized and not ready for implantation, it can be used can deliver a

controlled flow rate of 7-140 $\mu\text{l}/\text{min}$ to a cancerous tumor intravenously and will enable us to achieve Aim 4 of this project.



Figure 14: External pump module with control unit that will be used in future testing

The pump is set for maximum flow 140 $\mu\text{l}/\text{min}$ for a delivery tube diameter of 0.02". The flow rate can be altered by changing the potentiometer in the circuit (arrangements can be made to make this easily accessible). Another method to alter the flow rate is to change the interconnect tube dimensions. The flow rates for different tube dimensions are as shown in Table 1. The pump needs to be primed. That is, there should be some fluid injected in the tubing before the pump operation is started. Once the flow has been established this need not be repeated unless the fluid in the reservoir is depleted. The reservoir may be open or closed type. There are toggle switches with LED indicators for ON (RED) and OFF indication.

D. DRUG DELIVERY RATES

During this research, it will not be possible to implant our prototypes into Copenhagen rats for testing, due to their large sizes. Instead, we will connect the prototype through intravenous ports or directly to the tumor tissue, and control the drug delivery rate.

Drugs administered via conventional techniques target not only the diseased cells but also the healthy cells. Oral medications, injections and capsules are the most frequently used techniques. These techniques rely on blood flow to carry the drug to the targeted organ or cells. To ensure complete cure, the dosages required are higher and stronger and can have severe side effects. Methods to deliver a drug locally in order to make it more potent have been extensively studied and documented in the past. Gelatin coated pills, compressed pills minimized the side effect of drugs; however they still rely on the uptake of the drug into the circulatory system through the stomach and intestinal lining. Targeted or localized drug delivery using polymer stents, drugs coated with polymer that are biodegradable or water soluble have been proposed and have been approved for use in various treatments. The need to appropriate modulation of the delivery rate is required to maximize the therapeutic effects with low toxicity.

Drug delivery rates for drugs to be effective must maintain a specific level between the minimum required and maximum level below toxicity at all times during the course of administration. There are several factors that determine the rates at different stages of the disease. The drug dosage administration is as depicted in Fig. 15. The key parameters that should be optimized for drug delivery are a) selectivity of drug action b) interval between

administrations drug dose and c) probability that the next dose is administered at the appropriate time.

Chemical stability, reaction with drugs, body fluids and temperature effects are studied to determine the best suited materials. There exist standards for determining biocompatibility of polymers. For example, the biocompatibility tests for Polyethylene are given by the ASTM standards F981, F639, F755.

In the future, we intend to use Parylene as a bio-compatible material to coat the micropump and associated components. We will also validate the effectiveness of various cancer drugs to the therapeutic outcome through the use of our micropump.

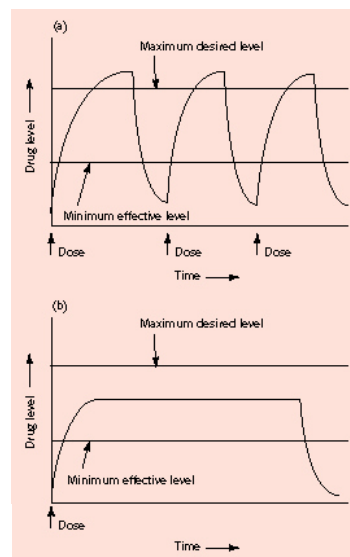


Figure 15: Drug levels in the blood with (a) traditional drug dosing and (b) controlled-delivery dose.

2. Progress on Aims 1, 2, 4, and 5 from co-PI Liu

A. INTRODUCTION

Co-investigator Liu is continuously collaborating with the PI Popa to better monitor drug effects to be delivered by the micro-pumps. She has also explored new research development to intraoperatively detect positive prostate cancer margins to guide laparoscopic prostatectomy. The clinical significance for such the development is given below:

Clinically localized prostate cancer is generally treated with either radiation therapy or surgery. Surgical treatment is currently undergoing a significant revolution; that is laparoscopic radical prostatectomy (LRP). This procedure permits complete removal of the prostate and seminal vesicles while minimizing pain and recovery. However, the laparoscopic approach greatly limits tactile sensation during the procedure. This is particularly true with robot-assisted LRP where no tactile feedback is available forcing the surgeon to rely solely on visual cues. Furthermore, the surgeon cannot evaluate the surgical specimen until the procedure is completed and prostate extracted. Though intraoperative frozen section pathologic analysis of a few select tissue fragments from the prostate or surgical site can be obtained, it is time consuming and costly. Concrete conclusions based on such samples are unreliable as they do not reflect the entire surgical margin status.

In recent years, a variety of optical spectroscopy techniques have been developed for detection and diagnosis of different kinds of cancers. However, most of these techniques mainly target luminal malignancies, such as cervical, colon, and esophageal cancers. Prostate cancer, on the other hand, is an intraparenchymal tumor that is commonly occurring in multiple places within the prostate gland. For early clinically localized prostate cancer, the most common presentation in 2006, it is not possible to visually identify the tumor during surgery, either within the prostate or at its capsular margin.

Therefore, it would be highly desirable to develop an integrated optical spectroscopic method that will allow the surgeon in real time to detect prostate adenocarcinoma both on the surface of the prostate and a few millimeters beneath the surface for accurate excision of the gland during laparoscopic prostatectomy. Such a technology that can reduce the incidence of positive surgical margins would significantly reduce prostate cancer recurrence and progression rates after surgery. The proposed development will enable surgeons to intraoperatively demarcate prostate cancer over the entire resected prostate so as to significantly reduce positive surgical margins and prostate cancer recurrence after surgery.

For this purpose, we have aimed at (1) the investigation of spectroscopic characteristics of light scattering, time-resolved auto-fluorescence, and NIRS of prostate cancer tissue using respective spectroscopic systems, and (2) the investigation of a multi-parameter assay (matrix) that consists of optical spectroscopic signatures of prostate cancer and can be used to classify the cancer surgical margins. Co-investigator Liu and her graduate students, along with her clinical collaborators from the University of Texas Southwestern Medical Center at Dallas, have made significant efforts in the last 8-10 months to explore the idea of developing an optical spectroscopic approach to intraoperatively detect positive prostate cancer margins by collecting preliminary data from the animal models and human prostate glands *ex vivo*. In this section, we present our preliminary study in the order of aims given above.

To obtain preliminary spectroscopic data from the human prostate glands immediately after prostatectomy, we utilized 3 different setups for reflectance spectroscopy and steady-state fluorescence measurements: **(1)** 3-channel diffuse (NIR) light reflectance measurement was performed with a hand-held probe having source-detector separations of 0.9, 1.5, and 2.2 cm ([Fig. 1a](#)); **(2)** a single-channel spectrometer (Ocean Optics, HRD-4000, [Fig. 1b](#)) was used for light-scattering reflectance spectroscopy with a needle-like probe having a source-detector separation of 0.5 mm (seen in [Fig. 1c](#)). **(3)** The same spectrometer was used along with a UV light source and a cut-off filter at 400 nm (to filter out the UV excitation) for steady-state fluorescence spectroscopy. For the single- and multi-channel spectrometers, the wavelength regions were 350-1100 nm and 350-900 nm, respectively.

We utilized the multi- and single- channel probes/spectrometers to measure the light reflectance from the surface of the intact resected prostate ([Fig. 1c](#)) to obtain the optical signatures under such a condition. However, to actually locate the prostate cancer, the prostate gland was bivalved for pathology analysis. Before fixing the prostate specimen, both light scattering and steady-state auto-fluorescence spectra were taken at multiple locations of the bivalved cross section ([Fig. 1d](#)). In some cases, prostate adenocarcinoma can be visually identified by the pathologist in several scattered small areas, as circled in [Fig. 1d](#). Confirmation of cancer came from the final pathology report, and [Fig. 1e](#) shows an example of irregular glands and clumps of cells, characteristic of prostate adenocarcinoma. Using the pathology report as a “gold standard,” we compared and characterized the light reflectance and auto-fluorescence data, and a few examples are given below.

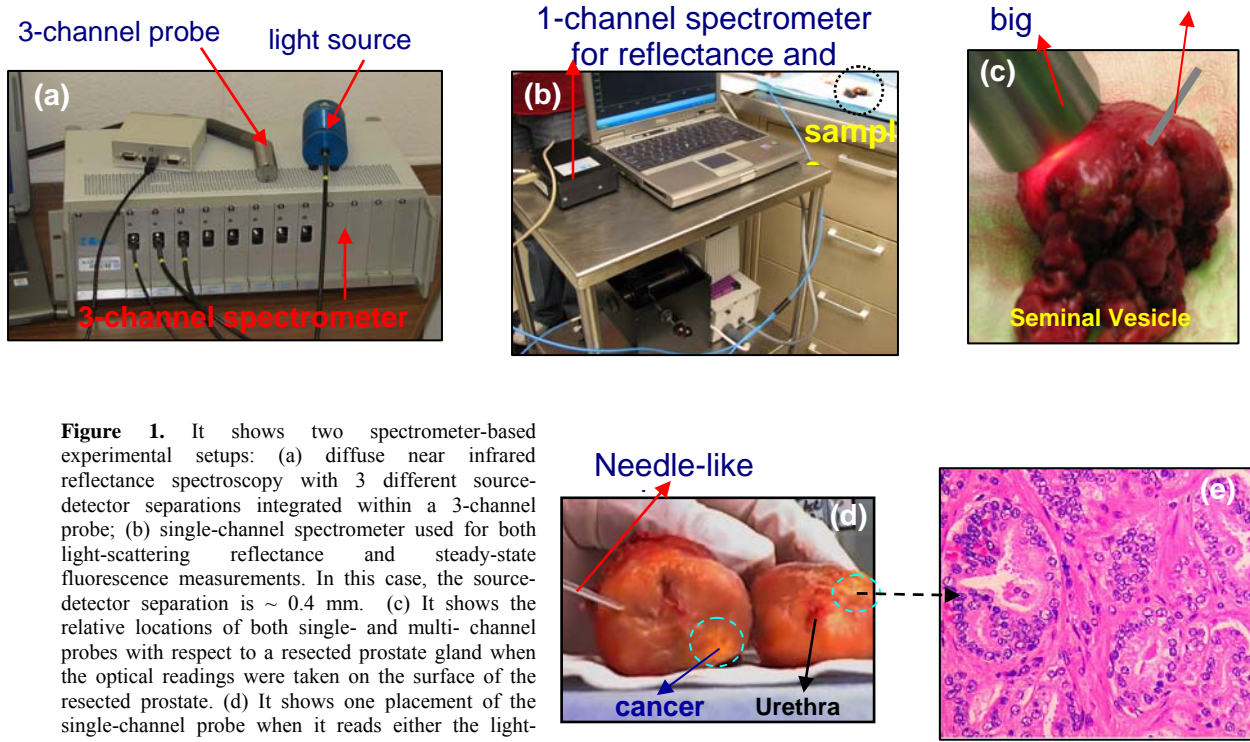


Figure 1. It shows two spectrometer-based experimental setups: (a) diffuse near infrared reflectance spectroscopy with 3 different source-detector separations integrated within a 3-channel probe; (b) single-channel spectrometer used for both light-scattering reflectance and steady-state fluorescence measurements. In this case, the source-detector separation is ~ 0.4 mm. (c) It shows the relative locations of both single- and multi-channel probes with respect to a resected prostate gland when the optical readings were taken on the surface of the resected prostate. (d) It shows one placement of the single-channel probe when it reads either the light-scattering reflectance or steady-state fluorescence after the resected prostate was bivalved. (e) It is a pathology image (with a magnification of $\times 10$ objective field) taken from a cancerous area, as labeled by a circle in (d).

B1. LIGHT SCATTERING REFLECTANCE FROM EX VIVO HUMAN PROSTATE

Figure 2 shows a few light scattering reflectance spectra taken from the bi-valved prostate cross section using the needle-like probe (Fig. 1d). The curves were calibrated with a white standard reflectance sample. After confirming with the pathology report, we recognized that the top three spectra in Fig. 2 were originated from healthy prostate gland areas and the bottom three from cancerous ones.

With multiple resected prostate glands measured and multiple sites used, we selected three particular spectral ranges: 440-500 nm, 545-560 nm, and 650-900 nm for data analysis to determine possible markers to distinguish prostate adenocarcinoma from normal gland tissues. Within those three ranges, we decided to use spectral slopes as indexes for comparison. Figure 3 shows an example taken from one prostate gland.

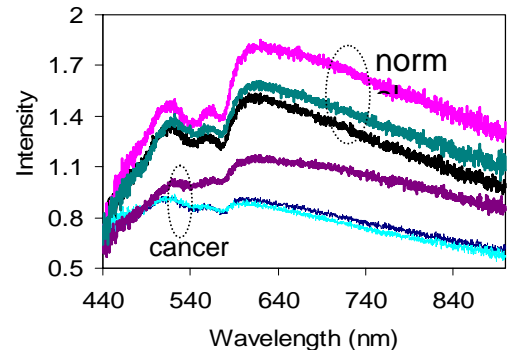


Fig. 2 light scattering reflectance of human prostate.

As seen in Fig. 3, the differences in all three indexes are significant ($p < 0.05$) between cancer and control tissues, particularly for indexes 2 and 3. The trends of these three indexes have been consistently seen in the other observed resected human prostate glands, and it may be reasonable to consider these parameters as putative diagnostic indices for prostate adenocarcinoma.

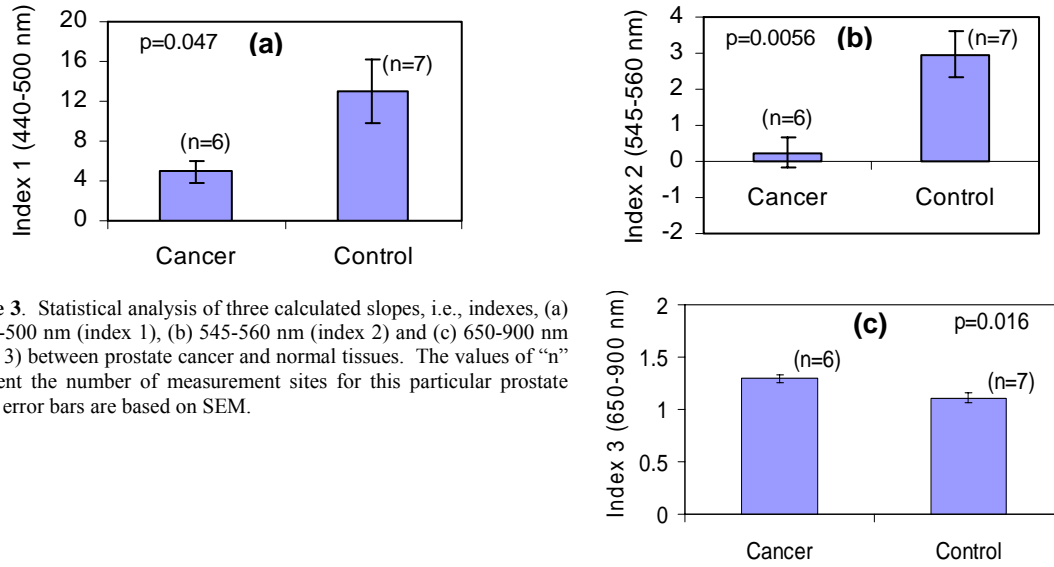


Figure 3. Statistical analysis of three calculated slopes, i.e., indexes, (a) at 440-500 nm (index 1), (b) 545-560 nm (index 2) and (c) 650-900 nm (index 3) between prostate cancer and normal tissues. The values of “n” represent the number of measurement sites for this particular prostate gland; error bars are based on SEM.

On the other hand, it is also important to know the spectral shapes of the light-scattering reflectance spectra obtained with the needle-probe from the prostate capsule surface (Fig. 1c). Figure 4a below shows several spectra taken under such a condition from the cancer and normal areas. All the curves are calibrated and normalized at 500 nm. Among all 5 spectra, only the thick black curve was taken from the normal area, but all the other 4 curves were taken from cancerous areas. Besides the common absorption feature of oxygenated hemoglobin at 500-600 nm, we noticed that all the spectra taken from the cancerous areas have higher light reflectance in the region of 600-900 nm. We interpret that this increase in light reflectance results from an increase in light scattering in the region of 450-900 nm. To confirm our interpretation, two blood-Intralipid tissue phantoms were created with two different scattering coefficients while keeping the same amount of hemoglobin concentration and oxygen saturation. Figure 4b plots the experimental data that were calibrated and normalized as Fig. 4a. It proves that a higher scattering medium exhibits a larger light reflectance spectrum. The increase in light scattering seen in Fig. 4a should result from the enlarged cell nuclei and increased cell densities that are often encountered in prostate cancer tissues.

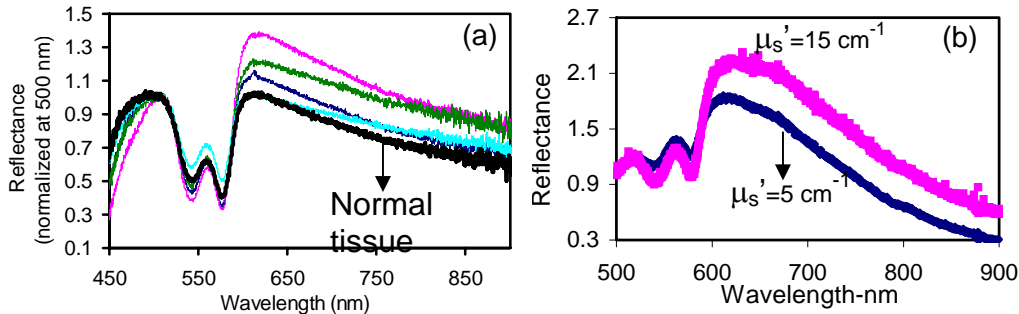


Fig 4. Calibrated and normalized light scattering reflectance spectra taken from (a) the surface of an intact resected prostate gland, only one spectrum being taken from the normal tissue (black curve), (b) blood-intralipid tissue phantom data taken with two reduced light scattering coefficients: namely, $\mu_s' = 5$ (in blue), $\mu_s' = 15 \text{ cm}^{-1}$ (in pink).

A recent theoretical development in light scattering is consistent with our previous work and further affords to quantify the optical properties of the measured sample using the light reflectance spectra. We plan to utilize this analytical expression for light reflectance to recover the optical and physiological parameters of the prostate adenocarcinoma in both *ex vivo* and *in vivo* studies.

B2. AUTO-FLUORESCENCE FROM EX VIVO HUMAN PROSTATE

Using a similar needle probe to the one used for the reflectance readings, we have measured auto-fluorescence from the bi-valved prostate cross section (Fig. 1d). The fluorescence excitation source was a broadband UV lamp with a cut-off filter at 400 nm that was placed in front of the lamp, so only 400 nm and shorter wavelengths can be delivered to the prostate specimen. The UV light was collimated and delivered to a bifurcated 1-mm fiber probe tip, and the detected auto-fluorescence was collected and sent to the single-channel spectrometer (Fig. 1b). While the detected spectral range was 350-1100 nm, we only focused our study in the UV-visible region, where NADH has a strong auto-fluorescence peak (at 460 nm). This portable fluorescence measurement system (Fig. 1b) was calibrated against a standard laboratory fluorometer before we processed the *ex vivo* prostate data.

Figure 5a shows two calibrated, steady-state autofluorescence spectra taken from a region of cancer and normal prostate gland, exhibiting a strong peak at 460 nm due to NADH. However, the two curves differ only in amplitude, no other distinct aspects between them. Then, we tried to combine the autofluorescence signals with the scattering reflectance (given in Fig. 4a) by either multiplying them (Fig. 5b) or dividing the fluorescence by the reflectance (Fig. 5c). As seen in both Figs. 5b and 5c, the spectroscopic features are still not very diverse between cancer and normal tissues, meaning that spectroscopically, the steady-state autofluorescence measurement is not an optimal choice for cancer differentiation since the spectral difference heavily relies on intensity changes. Another method that is more sensitive to intrinsic properties of tissues is highly desirable, and **fluorescence lifetime measurement may be a good candidate as cancer markers**.

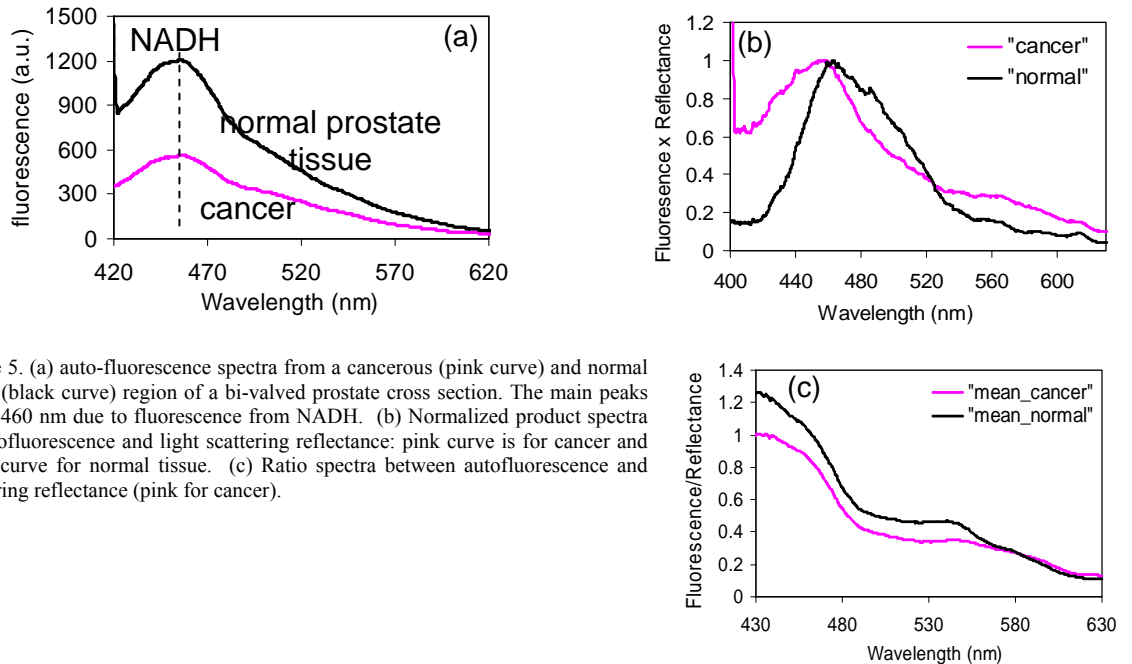


Figure 5. (a) auto-fluorescence spectra from a cancerous (pink curve) and normal tissue (black curve) region of a bi-valved prostate cross section. The main peaks are at 460 nm due to fluorescence from NADH. (b) Normalized product spectra of autofluorescence and light scattering reflectance: pink curve is for cancer and black curve for normal tissue. (c) Ratio spectra between autofluorescence and scattering reflectance (pink for cancer).

B3. NIRS TAKEN FROM EX VIVO HUMAN PROSTATE

Figures 6a and 6b are the diffuse reflectance spectra taken from an intact resected prostate gland ex vivo using the multi-channel, large source-detector separation probe (see Figs. 1a and 1c). The blue dotted symbols refer to the measured data, and the solid red lines are their respective diffusion theory fits. The diffusion-theory-based, spectrum-fitting algorithm has been very recently developed in the PI's research laboratory using water absorption as a reference to obtain initial fitting conditions. Our algorithm will be described in Section D. The data shown in this example were made with a separation of 1.5 cm. Specifically, Fig. 6a was obtained on the region that was devoid of any possible tumors on/near the surface, while Fig. 6b was made from the region as possible tumors indicated by the surgeon and pathologist. The fitted physiological and optical parameters are oxy-, deoxy-, total hemoglobin concentrations, water concentrations, and reduced light scattering coefficients (μ_s') from both regions, and those parameters are listed in the following Table.

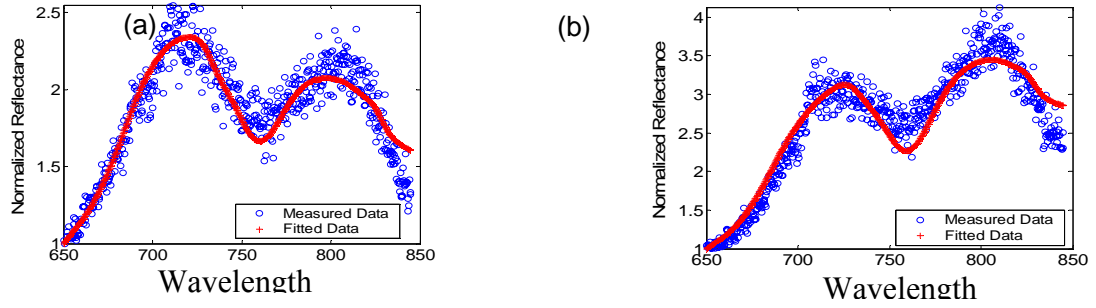


Figure 6: Comparison of reflectance spectra in the NIR region taken from (a) normal and (b) cancerous areas on a resected human prostate with their respective diffusion theory fits.

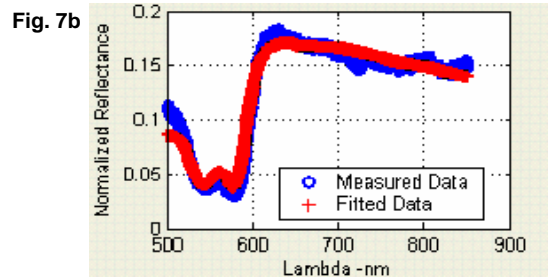
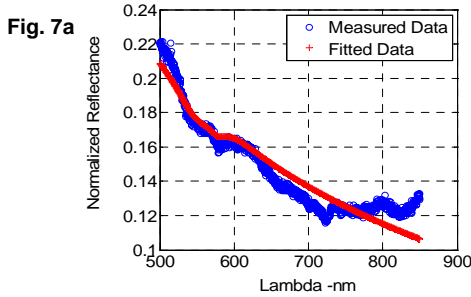
The data given in the Table are expressed in mean \pm SEM (standard error of mean). While more statistical analysis is needed to draw a reliable conclusion, it is seen primarily that the tumor regions have higher total and deoxy-hemoglobin, lower oxy-hemoglobin and water concentrations, perhaps larger light scattering, as expected and consistent with the reported literature for the prostate tumors.

1.5 cm Separation	[HbO] μ M	[Hb] μ M	[HbT] μ M	%H ₂ O	μ_s' (at 700 nm) cm ⁻¹
Tumor Regions (n=5)	34 \pm 7	34 \pm 3	68 \pm 10	68 \pm 2	11.5 \pm 0.7
Non-Tumor Regions (n=29)	38 \pm 3	26 \pm 3	64 \pm 5	72 \pm 1	11 \pm 0.7

B4. QUANTIFICATION OF PHYSIOLOGICAL PARAMETERS OF HUMAN PROSTATE GLANDS FROM THE LIGHT REFLECTANCE MEASUREMENTS

Recently we have advanced our quantification algorithm to quantify optical and physiological parameters of the human prostate gland using the reflectance spectra taken from the small source-detector probe. This advance is based on the newly published light scattering modeling work. Using the light reflectance model given by Zonios et al., we are able to fit the model to the light reflectance so as to quantify concentrations of oxygenated and deoxygenated hemoglobin, concentration of melanin, reduced light scattering coefficient at 450 nm, averaged light scattering size, and water concentration of the local measured area from the human prostate. Figure 7a shows a comparison between

the measured (blue symbols) and fitted (red curve) spectra, taken internally from a bi-valved region, which do not show strong hemoglobin features between 500-600 nm, whereas Fig. 7b is obtained externally from an intact excised human prostate with both measured and fitted data. The latter case exhibits a strong absorption dip due to hemoglobin existence. The table below lists all the fitted parameters obtained from the model curve fitting, showing that the optical and physiological parameters can be largely varied between the measurements obtained externally (Fig. 7b) and internally (Fig. 7a) from the same human prostate gland. This suggests that much more studies in quantifying optical and physiological properties of human prostate tissue, both healthy and cancerous tissues, be needed in order to develop optical signatures for prostate cancer identification or classification.



	HbO (micro Molar)	Hb (micro Molar)	Oxygen hemoglobin saturation (%)	Melanin (micro Molar)	Scattering parameter at 450 nm (cm ⁻¹)	Average Scattering Diameter (micron)	Water (%)
Fig. 7a readings	0.94	2.1	30.9	0.81	15.0	0.95	0.78
Fig. 7b readings	59.0	17.5	77.1	0.01	7.6	0.48	0.82

B5. LIGHT-SCATTERING REFLECTANCE AND AUTO-FLUORESCENCE FROM RAT PROSTATE TUMOR IN VIVO

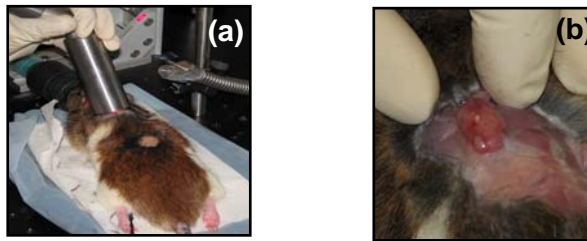
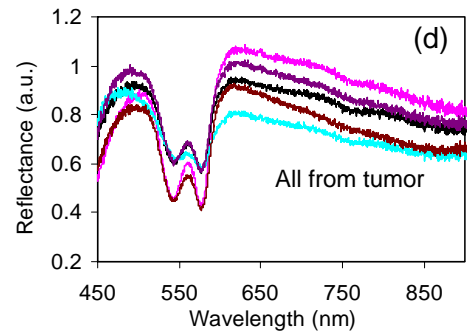
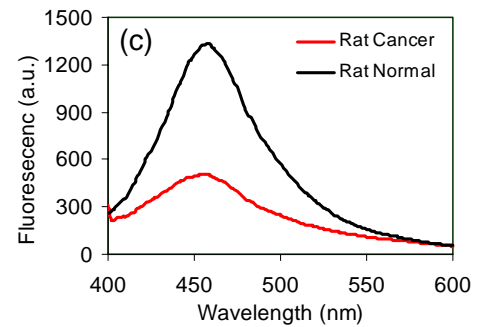


Figure 8. Photos of (a) a male tumor-bearing Copenhagen rat with the large-separation probe sitting on top of the prostate tumor, (b) an exposed living prostate tumor on the rat fore back. Both (c) steady-state autofluorescence and (d) light-scattering reflectance were taken from the exposed rat tumor to avoid the skin effect.



In the last 2 years, co-PI Liu has developed a rat prostate tumor model, under the support from the DOD Prostate Research Program, using adult male Copenhagen rats that were implanted with prostate carcinoma on the fore back (Figs. 8a and 8b). We have conducted our preliminary experiments on the animal tumors

of light scattering reflectance (Fig. 8d) and autofluorescence (Fig. 8c) using the needle-like probe, as well as the diffuse light reflectance with the multi-channel probe. By comparing Figs. 5a and 8c, also Figs. 4a and 8d, we noticed that the data from the human prostate tumor are very consistent with those taken from the rat tumor, and this conclusion holds for both light scattering reflectance and autofluorescence. This study also clearly demonstrates our ability to conduct animal tumor experiments.

B6. AUTO-FLUORESCENCE LIFETIME OF RAT PROSTATE TUMOR MEASURED IN VITRO

Co-Investigator Liu has recently collaborated with Dr. Gryczynskis from the University of North Texas Health Science Center at Fort Worth, who has applied the time-resolved technique to investigate the auto fluorescence lifetime of the rat prostate tumor tissues compared to the normal muscle tissues. Both types of tissues were removed from the rats a few hours before the measurements. The main advantage of the time-resolved fluorescence is that such measurements reveal intrinsic fluorophore photophysics parameters, which are intensity independent. For these preliminary measurements, we used a FluoTime200 fluorometer (PicoQuant, Inc.) equipped with pulsed light sources. Firstly, we were not sure that a weak pulsed laser would provide enough power to efficiently excite the tissue autofluorescence. Secondly, we did not know if the changes in observed lifetimes would be sufficient to distinguish the tumor samples from the normal. We selected the excitation of 375 nm hoping for efficient NADH/Flavins excitation.

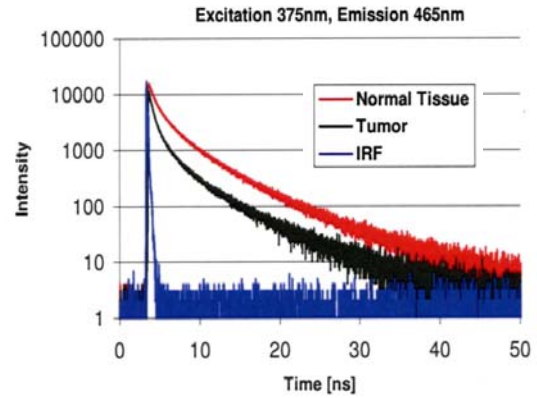


Fig. 9 Time-resolved auto-fluorescence data from both rat tumor and normal tissues.

We were positively surprised to detect strong fluorescence signals in the visible region of 440-550 nm. We could attenuate the signal by 100 fold using a neutral density filter with OD=2, and still collect high quality lifetime data. Thus, we do not expect any problem with the autofluorescence data collection in future time-resolved “Field” measurements in vivo. An example of the time-resolved tissue autofluorescence is presented in [Figure 9](#), where the **red** and black curves result from the normal and prostate tumor tissues, respectively. The **blue** sharp spike is the instrument response function. This figure clearly shows a significant lifetime decrease in tumor tissue. The autofluorescence intensity decays of the tissue can be approximated with the multi-exponential model, as given:

$$I(t) = \sum \alpha_i \exp(-t/\tau_i) \quad (1)$$

where τ_i are the decay times, α_i represent the amplitudes of the components at $t=0$. In this case, three components ($n=3$) were sufficient to fit the data with an acceptable confidence. The fractional contributions f_i of each decay time to the steady-state intensity is given by

$$f_i = \alpha_i \tau_i / \sum \alpha_j \tau_j. \quad (2)$$

Then, the average lifetime for multi-exponential decay is given by $\tau = \sum f_i \tau_i$. Another quantity, called amplitude-weighted lifetime, is given by $\langle \tau \rangle = \sum \alpha_i \tau_i$, which is proportional to the area under the curve.

The following Table provides a list of lifetime parameters analyzed using eqs. (1) and (2).

Observation (465 nm)	α_1	τ_1 (ns)	α_2	τ_2 (ns)	α_3	τ_3 (ns)	$\langle \tau \rangle$ (ns)	τ (ns)	χ_R^2
Normal	0.62	0.53	0.30	2.22	0.08	6.52	1.53 ^(a)	3.36 ^(b)	1.19
Tumor	0.73	0.35	0.22	1.51	0.05	5.83	0.86	2.49	1.01

$\alpha)$ $\langle \tau \rangle = \sum \alpha_i \tau_i$; $\beta)$ τ is the average lifetime and equal to $\sum f_i \tau_i$, $f_i = (\alpha_i \tau_i) / (\sum \alpha_i \tau_i)$

This table unambiguously demonstrates that both amplitude weighted lifetime and average lifetime, i.e., $\langle \tau \rangle$ and τ , are significantly different between the normal muscle tissue and prostate tumor tissue. This knowledge implies that both $\langle \tau \rangle$ and τ may be used as classification markers to identify prostate tumor from normal tissues. In short, we learned in this preliminary time-resolved study that decays in autofluorescence intensity from prostate cancer are easily detectable, and that time-resolved autofluorescence of the tissue is durable, carrying characteristic information on cancer. We are confident that a portable device for “Field” lifetime measurements can be constructed with a modest cost.

B7. NIRS OF RAT PROSTATE TUMOR IN VIVO

As mentioned earlier, the animal experimental data are very consistent with the human prostate cancer for both light reflectance and autofluorescence. Indeed, the diffuse NIR reflectance from the rat tumor displayed NIR spectra similar to Fig. 6a. Moreover, we inspected the data in the NIR region up to 1100 nm so as to examine the signals at dominant water absorption. Figure 10 plots apparent absorption, which is calculated by taking the logarithm of reciprocal reflectance. This experimental result clearly demonstrates that the prostate tumor has lower water and higher deoxy-hemoglobin concentrations than normal tissues, in good agreement with the report by Alfano et al.

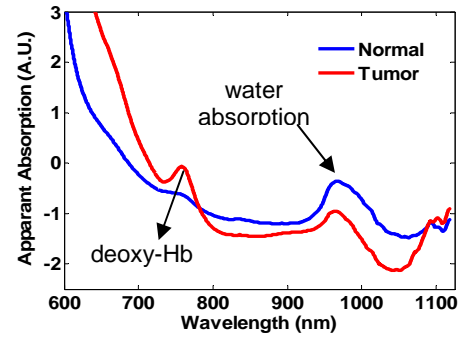


Fig. 10: Log of reciprocal reflectance

B8. CLASSIFICATION ALGORITHMS TO DEMARCAT PROSTATE CANCER

The Minimal Distance Method (MDM) is a statistical matching process commonly used in pattern recognition for remote sensing and image processing. Class assignment follows minimization of the Euclidan (linear) or Mahalanobis (correlated) distance. We have

found Mahalanobis distance to be useful being that it is scale-invariant and accounts for correlations within data sets. Furthermore, the Support Vectors Machine (SVM) has found great utility in machine learning. It is a supervised learning algorithm that recognizes subtle patterns contained in complex data sets. SVM is an effective classifier and has been used with increasing frequency in recent years.

We used both MDM and SVM for our classification algorithm tests. In parameter selections, we picked up to 10 parameters that were derived from light-scattering reflectance, autofluorescence lifetime, and diffuse NIR reflectance. These parameters are Index 1, index 2, index 3, $\langle\tau\rangle$, τ , HbO, Hb, HbT, μ_s' , and water concentration, labeled A1, A2, A3, B1, B2, C1, C2, C3, C4, and C5, respectively. In the simulated classification runs, we generated 240 uniform distributed sample points for each of A's, B's and C's with a uniformly distributed random numbers in the range of mean \pm S.D. For each set, 211 points were used to train the classifiers, and the rest 29 samples for each set were available for testing the performance of the classification algorithms. Next, we selected randomly 3 or 5 parameters (such as A1, A2, C1, C3, and C5) out of the 10 parameters to determine classification success rates in comparison to the rate with all 10 parameters used.

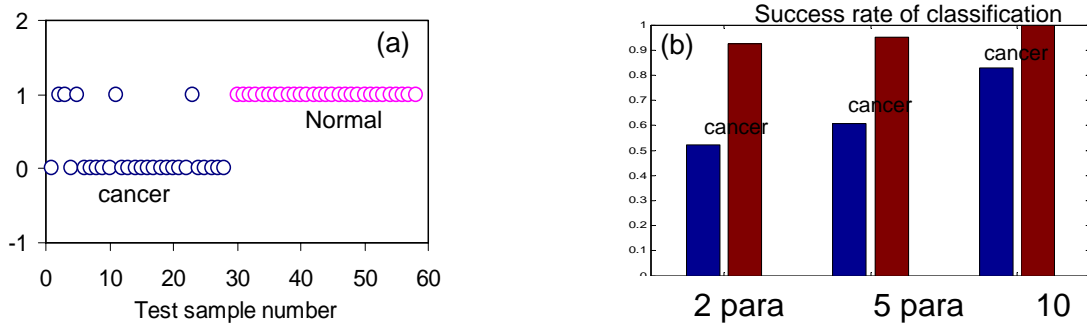


Figure 11. (a) Demonstration of classification for cancer and normal tissue using the SVM method. (b) summary of success rates using different number of parameters chosen from A's, B's, and C's. "para"=parameter.

Figure 11a shows an example how to label the classified tissue type: "1" for normal tissue and "0" for cancer. In this case, all normal tissues are correctly identified, while 5 out of 29 cases were missed for cancer, with a success rate of 100% and 83% for normal and cancer, respectively, namely, specificity is 100% and sensitivity is 83%. This set of data was obtained using SVM.

Among A's, B's and C's, to determine how many of them are needed to provide an accurate classification, we selected 45 sets of 2 parameters, 6 random sets of 5 parameters, and the complete set of 10 parameters and calculated the respective success rates, as shown in Fig. 11(b). It is clearly seen that more parameters do provide better accuracy in classification of both normal tissue versus cancer, while a further study to confirm the results and to improve the optimization approach is planned in the remaining work.

3. Progress on Aim 5 from co-PI Tang

In this project, we want to create appropriate cancer tumor animal models, that will guide the growth of cancer tumor in Copenhagen rats. These rats are then used to support all the experimental work in the project. For the past 2 years, we have successfully established reproducible prostate cancer animal model using cancer cell lines. Many of these animals have been used in the study of the development of imaging modality. Specifically, rat prostate cancer cell line R-3327-AT-3.1 was obtained from the American Type Culture Collection (Rockville, MA, USA). Cells were cultured in Dulbecco's Modified Eagle Medium DMEM supplemented with 10% Fetal Bovine Serum (Invitrogen, CA, USA) at 37°C in a 100% humidified atmosphere containing 5% carbon dioxide. The subcultivation ratio is 1:20 and the medium was changed every other day to ensure the fast growth of the cells. More details of our accomplishments have been reported in our 2005-2006 report.

In addition to this effort, for the past 12 months co-PI Tang has been focusing on developing alternate chemotherapeutic treatments based on Quantum Dots (QDs). Due to their strong luminescence even under hypoxic conditions and photostability, QDs has drawn intensive research effort for their use as a cell label in medical imaging. To improve the cancer tissue specificity, QDs have been developed to target tumor by active or passive targeting mechanisms. One of the seminal studies on active targeting showed that QDs labeled with the protein transferrin underwent receptor-mediated endocytosis in cultured HeLa cells. These studies have shown that conjugating the quantum dots with a suitable receptor facilitates intracellular uptake by receptor mediated endocytosis. In addition, most of the tumor cells have no specific markers. Furthermore, there are no specific markers which could be used to target all or most tumor cells. Thus, more efforts should be expended in developing passive cancer targeting strategies. Our recent studies have found that maximal cellular uptake of nanoparticles occurs with nanoparticles measuring around 100 nm in size (Nguyen et al., 2007). Based on these characteristics, our goal is to develop tumor targeting imaging probes by producing QDs embedded hydrogel particles (100 nm diameter).

Using a novel technology developed in our laboratory, we have been able to produce PNIPAM nanoparticles embedded with QDs and chemotherapeutic drugs. The functionality of these particles was then tested in vivo. Briefly, cancer cells (1×10^6 /0.1 ml/mouse) were implanted in Severe Combined ImmunoDeficient (SCID) mice. One week later, tumor tissues were observed on all the SCID mice back, with sizes of 0.5 to 1.0cm diameter. QDs (50ul) were injected into the tail vein of mice in one group while QD-NP with equivalent fluorescence intensity to QDs was injected in to the tail vein of mice belonging to the other group. Three hours following injection, the animals were sacrificed and the tumor tissue was explanted and embedded in OCT (Optimum Cutting Temperature) for histological analyses.

The H&E staining images of the tumor sections show that there are no morphological differences among tumor tissue treated with either QDs alone (Figure 1A) or QDs embedded particles (Figure 1B). There were no sign of inflammatory responses or

immune reactions. It suggests that both QDs particles and QD embedded particles are biocompatible. A closer look in to the tumor sections using a high magnification optical microscope showed a very scanty presence of luminescence in the case of QDs alone (Figure 1C) while a more intense luminescence was observed in the case of QDs embedded nanoparticles (Figure 1D). Since hydrogel nanoparticles can be incorporate with chemotherapy agents, we are in the processing of producing nanoparticles loaded with both QDs and chemotherapy drugs. It is our hope the this technology will simultaneously allow us to treat and to monitor tumor progression.

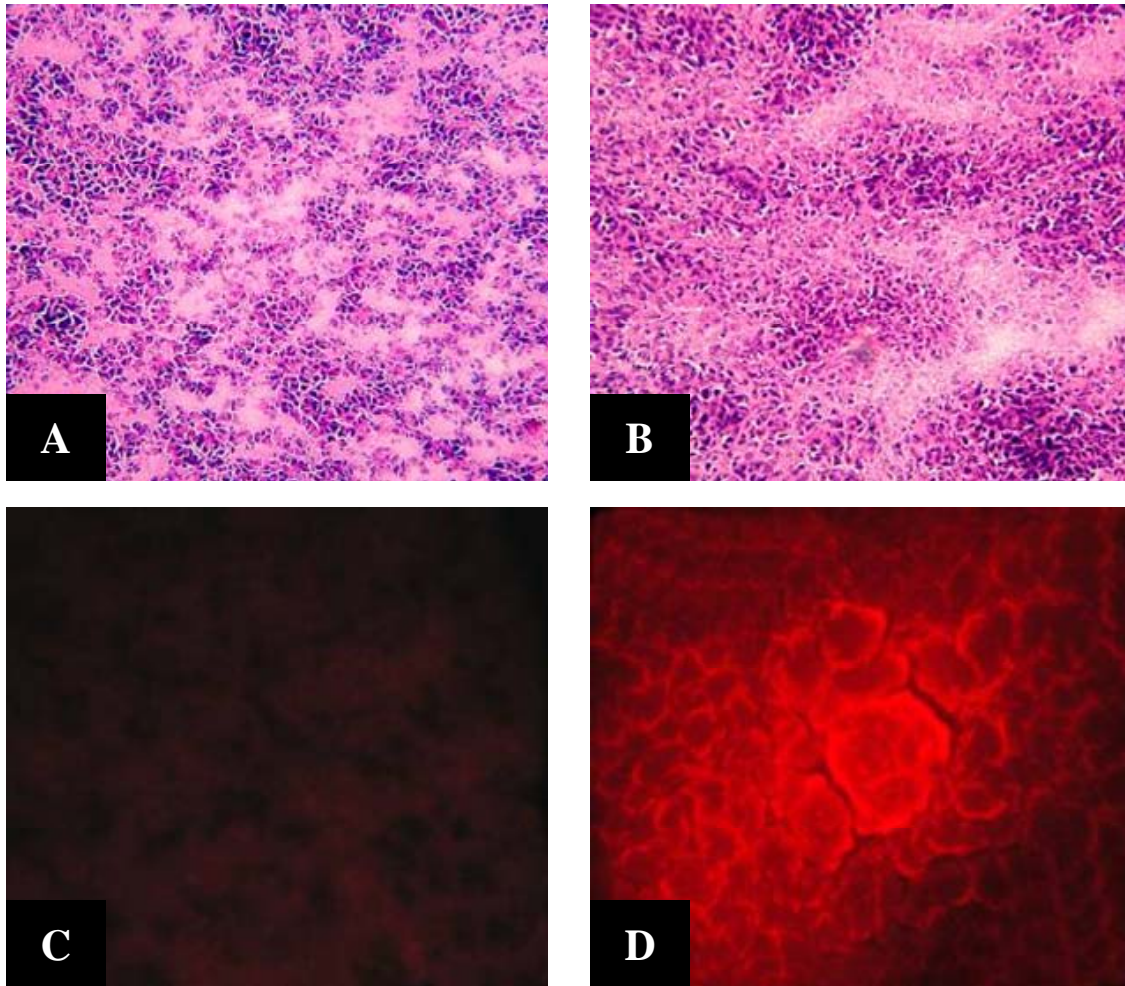


Figure 1 The H&E staining shows the similar morphology of tumor with quantum dots injected alone (A) and quantum dots embedded within nanoparticles (B) (Mag 20X). Quantum dots were observed under the fluorescence microscope; quantum dots injected alone in to the circulation are barely visible (C) while quantum dots embedded within nanoparticles are taken up in to the tumor and show up as bright red dots (D). (Mag 100X)

Key Research Accomplishments

- We have studied the micropump flow rate and thermal dissipation through FEA and lumped parameter models. Parts of the simulation model have been validated experimentally. The simulation models show drug delivery rates in the order of tens of milliliters per minute as required by cancer treatments with external pump units.
- We have refined fabrication and Level 0, 1, and 2 packaging processes for miniaturization of an implantable pump. A Level 2 prototype for drug delivery has been implemented. A complete finite-element analysis was performed in order to determine the impact of operating and design parameters like voltage, air gap thickness, substrate thickness, packaging and working fluid. All these parameters determine the maximum device temperature which in turn determines the maximum displacement and force of the diaphragm and the flow rate of the micropump.
- We have investigated the spectroscopic characteristics of
 - (a) light scattering,
 - (b) time-resolved auto-fluorescence,
 - (c) near infrared spectroscopyof human and animal prostate cancer tissue using respective spectroscopic systems. The measured parameters show great promises to be served as diagnostic markers for intraoperative detection of positive prostate cancer margins in laparoscopic prostatectomy.
- We also investigated two classification algorithms for identify positive prostate cancer margins by using a multi-parameter assay (matrix) that consists of optical spectroscopic signatures of prostate cancer and can be used to accurately classify the cancer surgical margins.
- Using a novel technology developed in our laboratory, we have been able to produce nanoparticles embedded with Quantum Dots and chemotherapeutic drugs.

Reportable Outcomes

During the third year, this grant supported several graduate students during their M.S. and Ph.D. studies. It supported the completion of a M.S. Thesis and a Ph.D. Thesis and the publication of several papers.

Journal Papers:

Nguyen KT, Shukla KP, Moctezuma M, Braden ARC, Zhou J, Hu Z, Tang L. In vitro studies of the cellular uptake of hydrogel nano- and micro- particles by phagocytes, vascular endothelial and smooth muscle cells. Journal of Biomedical Materials Research (in submission), 2007.

Conference papers:

1. Ashutosh Kole, Jeongsik Sin, Woo Ho Lee, Dan Popa, Dereje Agonafer and Harry Stephanou , “Design of Polymer Tube Embedded In-Plane Micropump,” IThERM, May 2006.
2. Kole, Ashutosh, Sin, Jeongsik, Lee, Woo-Ho, Popa, Dan, and Agonafer, Dereje, “Polymer Tube Embedded In-Plane Micropump for Low Flow Rate”, Proceedings of 24th Digital Avionics Systems Conference, Washington, D.C., October 30 – November 3, 2005 (not reported last year).
3. Smitha M. N. Rao, Saket Karajgikar, Jeongsik Sin, Dan Popa, Harry Stephanou, J.-C. Chiao, “Progress in the Development of the MEMS-Based In-Plane Micropump: Experimental Motion Characterization”, TexMEMS VII Conference, Dallas, October 2006.
4. Manan Goel, Harsha Radhakrishnan, Liping Tang, and Hanli Liu, “Application of Near Infrared Multi-spectral CCD Imager to Determine the Hemodynamic Changes in Prostate Tumor.” presented at Biomedical Optics Topical Meeting, Fort Lauderdale, Florida, March 19-23, 2006.
5. D. Kashyap, D. L. Peswani, J. Cadeddu and H. Liu, “Heterogeneities in Concentrations of Hemoglobin Derivatives and Oxygen Saturations in Human Prostate Tumors Evaluated by NIRS,” presented at Houston Society for Engineering in Medicine and Biology (HSEMB 2007) February 8, 2007.
6. Dheerendra Kashyap, Nguenvu Chu, Aditya Apte, BoPing Wang, and Hanli Liu, “Development of broadband multi-channel NIRS (near-infrared spectroscopy) imaging system for quantification of spatial distribution of hemoglobin derivatives,” Proc. SPIE Int. Soc. Opt. Eng. 6434, 64341X (2007).

M.S. Thesis and Ph.D Dissertations:

Manan Goel, “Development and Application of Near Infrared CCD Imager to Monitor Hemodynamic Changes in Prostate Tumor During Chemotherapy,” MS thesis, The University of Texas at Arlington, Arlington, TX, August 2006.

Dheerendra Kashyap, “Development of a Broadband Multi-Channel Near Infrared Spectroscopic System for Quantifying the absolute Concentrations of Hemoglobin Derivatives,” Ph.D. The University of Texas at Arlington, Arlington, TX, dissertation, May 2007.

Invited Talks:

Hanli Liu, “Recent Development on Novel Applications of Optical Spectroscopy and Imaging for Clinical Applications,” Beckman Laser Institute, UC Irvine, Irvine, CA, Sept. 14, 2006.

Hanli Liu, “Non Invasive and Minimally Invasive Characterization of Tumor Using Optical Methods,” Texas Cancer Registry, Texas Department of State Health Services, Mini-Educational Regional Conference, Fort Worth, Texas, July 14, 2006.

Patent Application:

Title for the patent: “Optical Methods to Intraoperatively Detect Positive Prostate Cancer Margins.”

Time to file the patent: May 2007.

Current status: UTA is reviewing the patent application.

Students supported:

Radhakrishnan, Harsha, 06/07 - 09/06

Goel, Manan, 6/06 – 09/06

Nair, Ashwin, 06/06 – 06/07

Rao, Smitha, 06/06 – 06/07

Karajgikar, Saket, 09/06-06/07

Prajapati, S, 01/07-06/07

References

- [1] George Zonios and Aikaterini Dimou, "Modeling diffuse reflectance from semi-infinite turbid media: application to the study of skin optical properties," *OPTICS EXPRESS* Vol. 14(19) 8661-8674 (2006).
- [2] W. B. Wang, J. H. Ali, M. Zevallos, and R. R. Alfano, "Near infrared imaging of human prostate cancerous and normal tissues based on water absorption", in OSA 2004 Biomedical Optics Topical Meetings on CD-ROM (The Optical Society of American, Washington, DC, 2004), MF 38.
- [3] http://www.thermo.com/com/cda/resources/resources_detail/1,2166,13324,00.html
- [4] <http://www.homepages.informatics.ed.ac.uk/rbf/HIPR2/classify.htm>
- [5] Cortes C and Vapnik V "Support-vector networks," *Machine learning*, 20, 273-297, (1995).
- [6] Tamayo P, Slonim D, Mesirov J, Zhu Q, kitareewan S, Dimitrovsky E, Leander E, and Golub T, "Interpreting patterns of gene expression with self-organizing maps," *Proc. Natl. Acad. Sci. USA*, Vol. 96, 2907-2912, (1999).
- [7] Furey TS, Cristianini N, Duffy N, Bednarski DW, Schummer M, and Haussler D, "Support vector machine classification and validation of cancer tissue samples using microarray expression data," *Bioinformatics*, Vol. 16 (10), 906-914, (2000).
- [8] Vapnik VN, "The Natural of Machine Learning Theory", Springer-Verlag, New York, (1999).
- [9] Burgers CJC, "A tutorial on support vector machine for pattern recognition", *Data Mining and Knowledge Discovery*, 2(2), 121-167, (1998).
- [10] Cristianini N and Shawe-Taylor J, "An Introduction to Support Vector Machines," Cambridge University Press, Cambridge, 2000.
- [11] Cortes C and Vapnik V, "Support-vector network," *Machine Learning*, 20, 273-297, (1995).
- [12] D J Laser, J G Santiago, "A review of micropumps," *Journal of micromechanics and microengineering*, Vol. 14, 2004.
- [13] Linnemann, P. Woias, C.-D. Senft, and J.A. Ditterich, "A self-priming and bubble tolerant piezoelectric silicon micropump for liquids and gases," *Proceedings on The Eleventh Annual International Workshop on Micro Electro Mechanical Systems*, pp. 532-537, 1998.
- [14] C. Grosjean and Y.-G. Tai, "A thermopneumatic peristaltic micropump," *International conference on solid state actuators and sensors*, 1999.
- [15] W.L. Bernard, H. Kahn, A.H. Heuer, and M.A. Huff. "Thin-Film Shape-Memory Alloy Actuated Micropumps," *J. MEMS*, Vol. 7, 245, 1998.
- [16] J.G. Smits. "Piezoelectric micropump with microvalves," *Proc. 8th University/Government/Industry Microelectronics Symposium*, 92, 1989.
- [17] J.G. Smits. "Piezoelectric micropump with three valves working peristaltically," *Sensors & Actuators A*, Vol. 21, 203, 1990.
- [18] J.A. Folta, N.F. Raley, E.W. Hee. "Design, fabrication and testing of a miniature peristaltic membrane pump," *5th Technical Digest Solid-State Sensor and Actuator Workshop*, 186, 1992.
- [19] J. Sin, W.H. Lee, H. E. Stephanou, "In-Plane Micropump: design Optimization," *Proc Nanotech*, Vol. 1, 2004.
- [20] Dimitrios K Filippou, Christoforos Tsikkinis, Georgios K Filippou, Athanasios Nissiotis and Spiros Rizos, "Rupture of totally implantable central venous access devices (Intraporcs) in patients with cancer: report of four cases," *World Journal of Surgical Oncology*, 2004.
- [21] Implantable medical applications of lithium-ion technology Rubino, R.S.; Gan, H.; Takeuchi, E.S.; *The Seventeenth Annual Battery Conference on Applications and Advances*, 2002.
- [22] Lithium ion batteries for medical devices Spillman, D.M.; Takeuchi, E.S.; *The Fourteenth Annual Battery Conference on Applications and Advances*, 1999.
- [23] J. H. Schulman, J. P. Mobley, J. Wolfé, E. Regev, C. Y. Perron, R. Ananth, E. Matei, A. Glukhovskiy, R. Davis, "Battery Powered BION FES Network," *Proceedings of the 26th Annual International Conference of the IEEE EMBS*, 2004
- [24] Akin T, Najafi K and Bradley R M, "A wireless implantable multichannel digital neural recording system for a micromachined sieve electrode," *IEEE Trans. Solid-State Circuits* **33**, 1998.
- [25] Ashutosh Kole, "Polymer Tube Embedded In-plane Micropump: Design, Analysis and Fabrication," Master's Thesis, Univ. of Texas at Arlington, 2005.
- [26] "BIOMATERIALS: Polymers in Controlled Drug Delivery," Lisa Brannon-Peppas, *Medical Plastics and Biomaterials Magazine*, November 1997.
- [27] "Growth factor delivery in tissue engineering," W.M Saltzman, *MRS Bulletin*, 1996.
- [28] "Materials for protein delivery in tissue engineering," Samuel P. Baldwin, W.M Saltzman,, *Advanced drug delivery reviews*, 1998.
- [29] "Drug DeliveryMarket Summary," *Nusil Silicone Technology*, White paper.
- [30] "Controlled drug delivery: therapeutic and pharmacological aspects," J. Urquhart, *Journal of internal medicine*, 2000.
- [31] "Silicones as a Material of Choice for Drug Delivery Applications," Brian Reilly, Stephen Bruner, NuSil Technology, *Presented at 31st Annual Meeting and Exposition of the Controlled Release Society*, June 12 – 16, 2004.
- [32] Bell, D. J., Lu, T. J., Fleak, N. A., and Spearing, S. M., "MEMS actuators and sensors: observation on their performance and selection for purpose," *J. of Micromechanics and Microengineering*, 15, 2005.
- [33] Laser, D. J. and Santiago, J. G., "A review of micropumps", *J. of Micromechanics and Microengineering*, 14, 2004.
- [34] Drug delivery systems through 2007- Market size, market share, market leaders, demand forecast, sales, company profiles, market research, industry trends.

- [35] N. T. Nguyen, and S. Wereley, "Fundamentals and Applications of Microfluidics," Artech house Publication, ISBN 1-58053-343-4, 2002.
- [36] Sin, J., Lee, W. H. and Stephanou, H. E., "In-plane micropump: design optimization", Technical proceedings of the NSTI Nanotechnology conference and Trade show, Vol. 1, 2004.
- [37] Huang, Q-A. and Lee, N. K. S., "Analysis and design of polysilicon thermal flexure actuator," J. of Micromechanics and Microengineering.9, 2005.
- [38] Reithmuller, W. and Benecke, W., "Thermally excited silicon microactuators," IEEE Transactions for Electronic Devices, 1998.
- [39] Guckel, H., Klein, J., Christen, T., Skrobis, K., Lnadon, M. and Lovell, E. G., "Thermo-magnetic metal flexure actuators," Technical Digest IEEE Solid State Sensor and Actuator Workshop, 1992.
- [40] Lin, L. and Chaio, M., "Electrothermal Responses of Lineshape Microstrcutres," Sensors and Actuators A 55, 1996.
- [41] Mhatre, A. "Implantable drug delivery system with an in-plane micropump," Master's Thesis, University of Texas at Arlington, 2005.